Thermal experimental investigation of radiative heat transfer for the validation of radiation models

N. P. Lavery, M. R. Vujičić & S. G. R. Brown
Materials Research Centre, School of Engineering,
University of Wales Swansea, U.K.

Abstract

The computation of the fraction of the thermal radiation power that leaves one surface and arrives at another, ultimately requires the determination of the geometrical view factors for radiation modelling. Several methods for the calculation of geometrical factors are available, including contour integration, Monte Carlo and the Hemi-Cube methods. Analytical test cases are available as benchmarks of the view factor, such as for the well-known parallel plates case, which allow modellers to validate their geometrical factor routines. However, there are no analytical solutions that simultaneously combine view factor information with conductive and radiative heat transfer effects.

This paper describes the construction of a simple test rig that allows experiments to be performed with emphasis on measuring the radiative heat transfer to benchmark coupled conduction and radiation heat transfer models in which convection aspects are of less importance. The equipment has been used to look at various heat transfer cases, such as, between parallel plates, between inclined hinged plates and the thermal effects of third surface shadowing. The models developed incorporate the Finite Element method and numerical methods for the view factor calculation. The results of these experiments are presented as benchmarking data for other model users and developers.
Keywords: Monte-Carlo view factors, experimental data, finite element, radiative and conductive thermal model.

 © 2005 WIT Press
www.witpress.com, ISSN 1743-355X (on-line)

1 Introduction

Of the three modes of heat transfer, radiative models particularly difficult to validate as there are no analytical solutions and basic experimental data is difficult to find, possibly because of the issues with decoupling convective and conductive modes in experiments.

The primary application for the solver described herein is to the prediction of external thermal distributions by conjugate heat transfer in airframes from internal heat sources, such as from jet-pipes and exhaust sections, in both fixed wing and rotary wing aircraft, but could equally well be used for land- and sea-based vehicles. The specific radiative heat transfer of this model has its emphasis on the reflective and emissive properties of the surfaces, assuming a semi-steady state of convective heat flow and minimal radiative inter-flow participation. A description of the progress of the development can be found in past papers, [1], [2] and [3].

To deal with the three-dimensional, complex geometries (including internal cavities) of such applications, the finite element method was chosen with a fast matrix solver to maximise efficiency. Throughout the project, a number of experimental rigs have been constructed, and this paper gives details of one particular experimental rig which was constructed with the specific purposes of validation for the radiative heat transfer mode.

2 Governing equations and numerical model

2.1 Conduction

Fourier's second law of heat conduction in a solid can be written as, [4],

$$\rho\, C_p \frac{\partial T}{\partial t} = k\left(\frac{\partial^2 T}{\partial x^2} + \frac{\partial^2 T}{\partial y^2} + \frac{\partial^2 T}{\partial z^2}\right) + Q \tag{1}$$

In eqn (1), T is the temperature, ρ is the density, C_p is the specific heat capacity, k is the thermal conductivity and Q is a heat source term which can include flux contributions from radiation and/or convection boundary conditions at internal and external surfaces of the volume.

2.2 Surface to surface radiation

The Stefan-Boltzmann equation for diffuse-gray radiative heat flux between two surfaces is given by,

$$q_{i\to j} = F_{i\to j}\sigma(\varepsilon_i T_i^4 - \alpha_j T_j^4) \tag{2}$$

In Eqn (2), $q_{i\to j}$ is the heat flux, $F_{i\to j}$ is the geometrical view factor from surface i to surface j, σ is the Stefan-Boltzmann constant, T_i is the temperature of surface i, T_j is the temperature of surface j, ε_i is the emissivity of surface i

 © 2005 WIT Press
www.witpress.com, ISSN 1743-355X (on-line)

and $\alpha_j = \varepsilon_j$ by Kirchoff's law, is the absorptivity of surface j. View factors are calculated by various numerical methods, as described in section 2.5

2.3 Convection

Convection can be dealt with by using heat transfer coefficients (HTC) at surfaces as boundary conditions, which can also be imported from commercial Computational Flow Dynamics (CFD) codes (currently FLUENT and PHEONICS).

2.4 Finite element solution technique

A transient, standard Galerkin finite element method is used, [5], [6], in which volumes are divided into linear hexahedral elements and Eqn (1) takes on a discrete matrix form solvable by a computer.

Various solvers have been implemented to invert the matrices, however, the most efficient in terms of both storage and time to solution, has been found to be the pre-conditioned conjugate gradient (PCG) algorithm.

2.5 View factor calculations

Initially, three direct methods for view-factor (VF) calculation were implemented based on the work of Shapiro [7]. These methods calculate view-factors of one element face with respect to another by integrating the view factor equations round each element face.

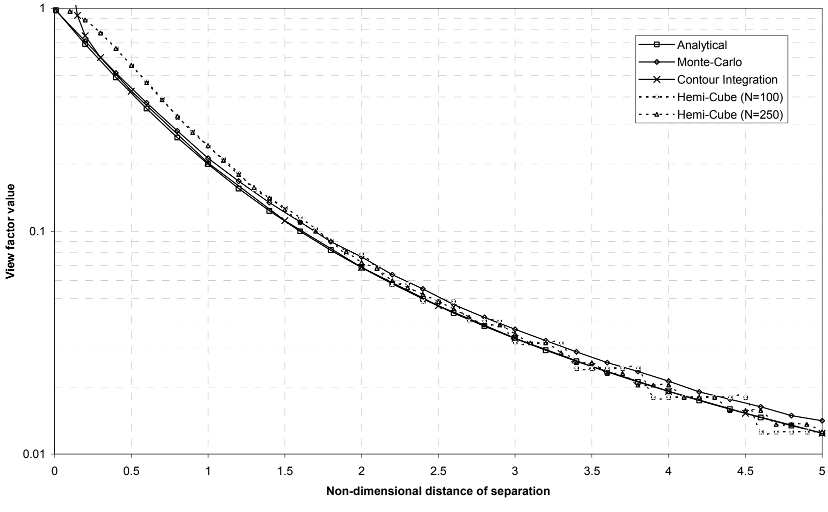

Figure 1: VF for parallel plates.

Two ray tracing methods have now also been implemented, namely the Monte-Carlo and Hemicube algorithms, as described in [8]. The Monte-Carlo method works by sending out rays in random directions from an element face and keeping tabs on the number of times that the ray strikes another surface. The Hemicube method is similar but works by setting up half a unit cube on each element face, which is sub-divided into "pixels", and sending out rays in a structured manner from the centre of the elements face, and each time an opposing face is struck, an equation is used to increment the value of the VF.

The numerical and analytical (see [8]) VF values for parallel plates are plotted in Figure 1 for 1mx1m plates, as a function of increasing separation distance.

The numerical (Monte-Carlo) and analytical VF for hinged plates are plotted as a function of aspect ratios of the sides in Figure 2, errors are so small that they are visually imperceptible on this graph.

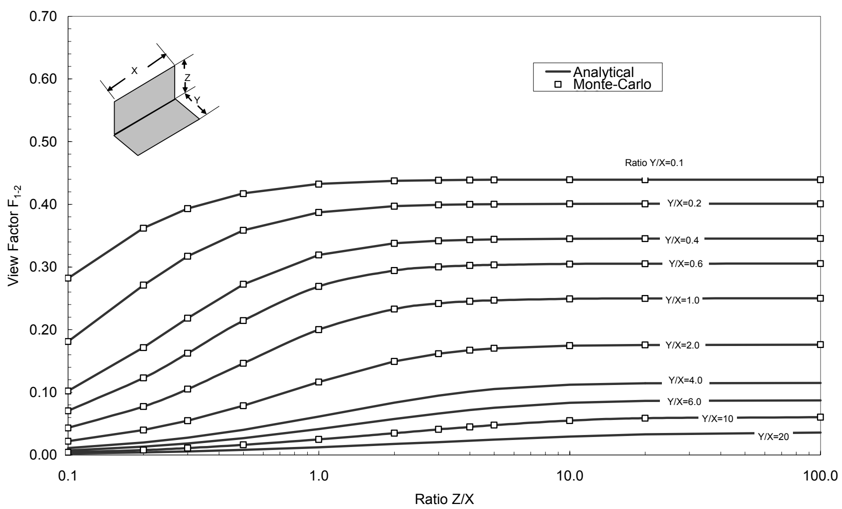

Figure 2: VF for hinged plates.

An error estimate was derived as the percentage difference between analytical and numerical values and is plotted in Figure 3 for various numerical methods.

While the contour integration method for VF calculation was extremely accurate on a face-by-face basis over most separation distances, it is not a ray tracing method and the only way of introducing shadowing effects is a costly re-search of all obstructing third-surface faces during the integration procedure.

The Hemicube method was found to be able to describe shadowing, but introduced unacceptable errors over small distances of separation and was not particularly accurate for larger separation distances, scaling poorly with the number of pixels used.

As can be seen in Figure 3, by far the most useful method was the Monte-Carlo based method which had most predictable errors throughout the range of problems tested.

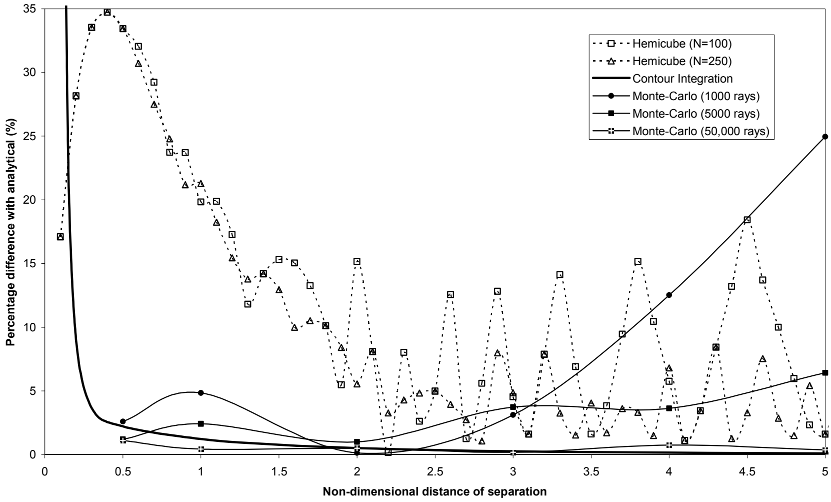

Figure 3: View factor error.

3 Experiment and numerical validation

The experimental test rig consists of an emitting heating element and a receiving plate, placed on rails which allow the distance of separation to be varied. The emitter and the receiver can be varied in shape (e.g. circular or square), and receiving plates made from aluminium, steel or brass, of various thicknesses (5-15 mm) can be used, although for the experiments described in this paper, only the steel plates were used.

The steel was coated with black high-emissivity paint, as were the walls of the containing box, itself made from wood. Thermo-couples were attached to both the receiver and the emitter. As can be seen in Figure 4, a thermal imaging camera was also used to capture thermal distributions. Thermal insulating wool was padded around the sides of the receiver to minimise convective heat loss.

For square plate receivers, the dimension of one side, L was 197 mm, while for the circular emitter, a diameter, D of 182 mm was used, and experiments were classified according to the distance separating the emitter and the receiver, C.

The layout for the current experimental rig was chosen based on the experience of previous experiments so that natural convection, although unavoidable without resorting to the use of a vacuum chamber, would be minimised by the placement of the plates vertically in the path of the radiated heat transfer. This meant that by far the maximum contribution to heating of the receiving element was from radiated heat, however, the current set-up was found to suffer heavily from daily ambient variations in the laboratory.

For the purposes computer modelling, material properties used are listed in Table 1.

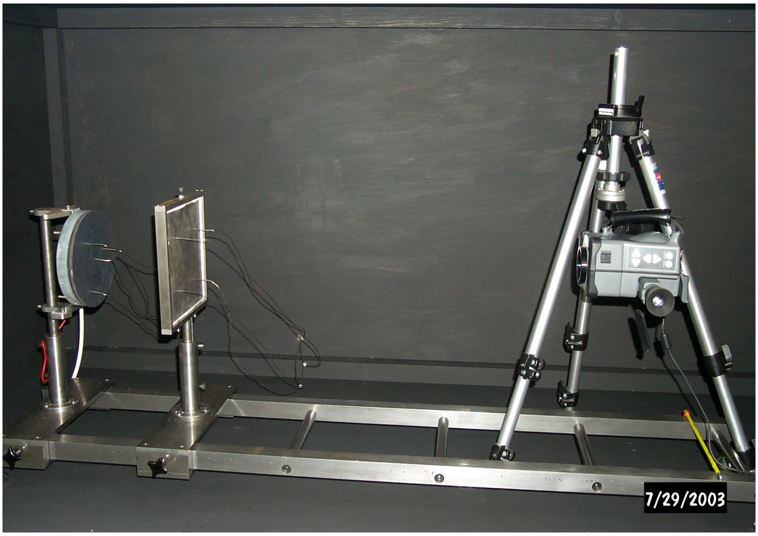

Figure 4: Experimental rig set-up.

Table 1: Material properties.

Material	Density kg/m^3	Emissivity	Specific heat capacity J/kg K	Conductivity W/m K
Steel AISI 304	8030	0.85	503	16.27

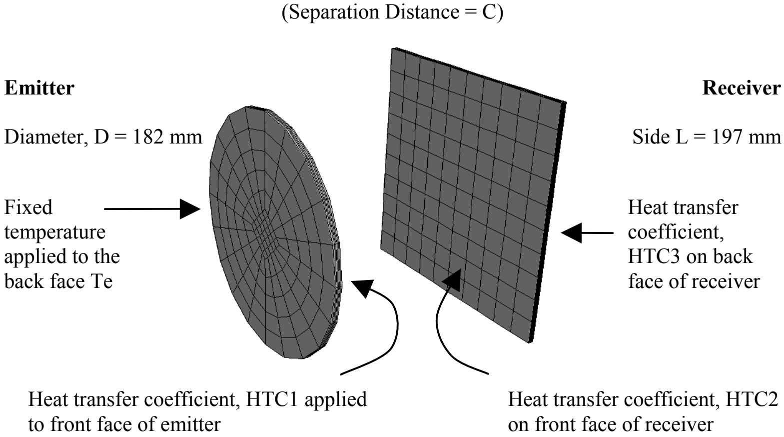

Figure 5: FE Mesh and boundary conditions.

3.1 Experiment 1 - circular emitter to square receiver

A typical FE mesh to simulate this experiment, and the boundary conditions applied are shown in Figure 5.

The heat transfer coefficients values were calculated from film theory of vertical heated plates, see [4], and calibrated with the experimental values to ambient temperature based on average plate surface temperatures. Actual values used are shown in Table 2, where Te, Tr1 and Tr2 are the measured average temperatures of the front face of the emitter, front face of the receiver and back face of the receiver, respectively, at steady state. And the heat transfer coefficients HTC1, HTC2 and HTC3 are defined in Figure 5.

The model compares well for the emitter throughout most time steps, but tends to underestimate the receiver in the preliminary time steps, as can be seen in the typical time-temperature graph shown in Figure 6. This could be due to the flux terms defined by eqn (2) of the model assuming a radiative balance at each time step, which in fact only occurs close to steady state.

Table 2: Experiment 1 data.

C/D	Te (K)	HTC1 (W/m^2K)	Tr1 (K)	HTC2 (W/m^2K)	Tr2 (K)	HTC3 (W/m^2K)	Ambient Temp (K)
0.2	740	7.9	489	6.5	466	6.4	295.8
0.5	720	7.8	424	6.0	407	5.8	291.3
1.0	710	7.7	365	5.2	357	5.1	291.2
2.0	710	7.7	309	3.6	308	3.5	293.3
4.0	709	7.7	309	3.6	309	3.5	290.7

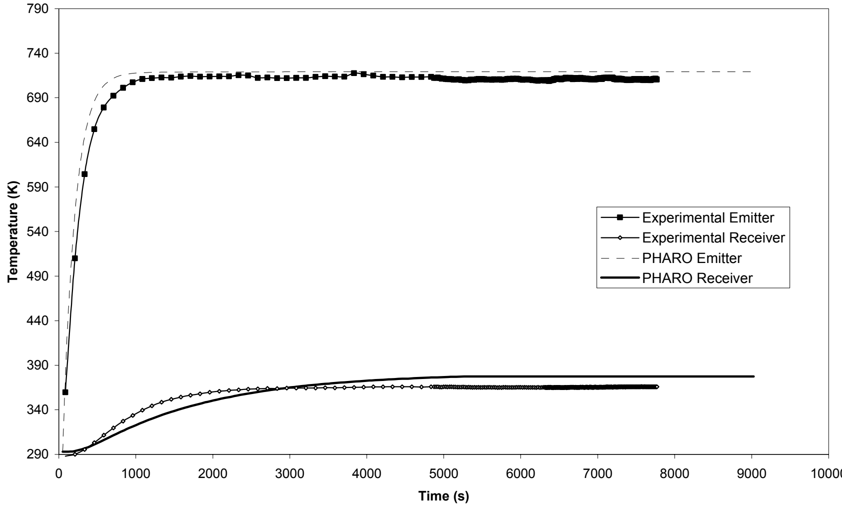

Figure 6: Transient results for disk to plate at C/D=1.0.

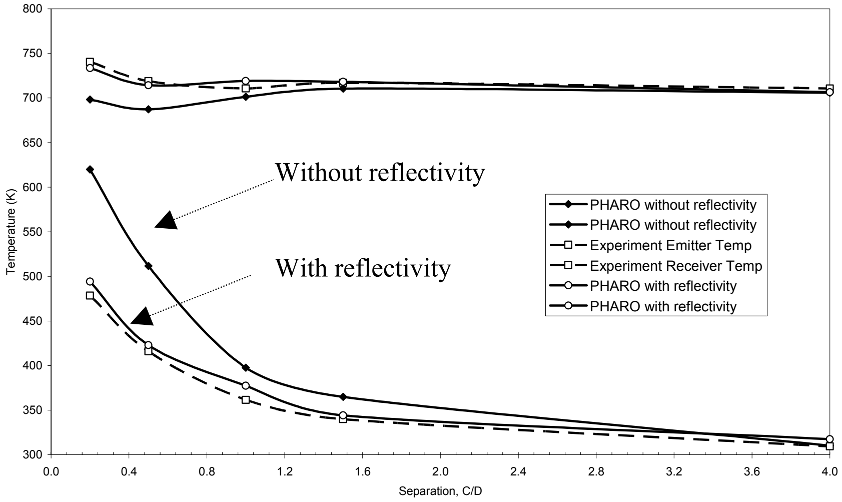

Figure 7: Steady state disk to plate results.

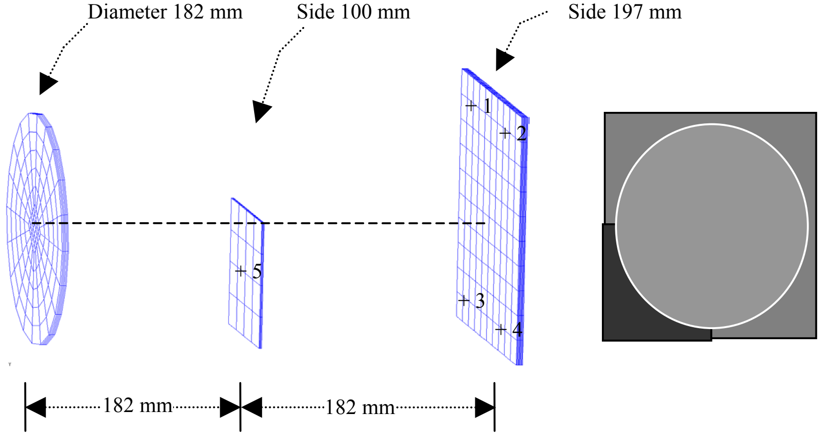

Figure 8: Shadowing geometry.

Without reflectivity, the model tends to underestimate the temperatures of the emitter and overestimate the temperatures on the receiver, as shown in Figure 7, particularly when the two are close together. Running the model with reflectivity gave temperature values very much closer to the experimental values over all separation distances.

3.2 Experiment 2 - shadowing effects from an obstructing surface

To examine shadowing effects, a steel obstructing square plate of side 100 mm and thickness 2 mm was aligned with the lower left hand corner of the receiving plate, as shown in Figure 8, and placed midway between the emitter and the receiver.

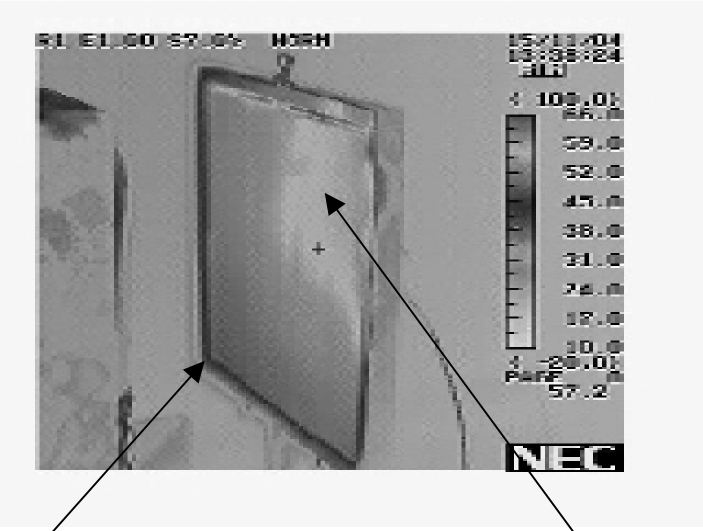

Figure 9: Thermal image (°C).

Coolest spot (3)

Hottest spot (2)

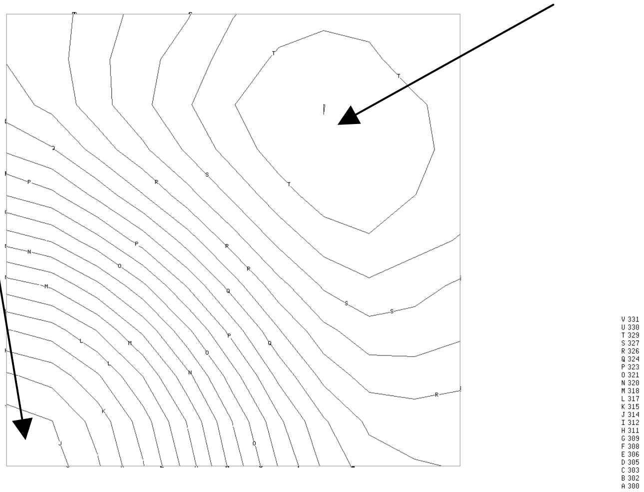

Figure 10: Temperatures (K).

For the thermocouples indicated in the same figure, the experimental results are summarised in Table 3

The simulation used the same heat transfer coefficients and material properties as given in the previous section. As can be seen from table 3, although the model prediction is about 10K out per thermocouple, trends are similar, i.e. both the locations of the coolest (3) and the hottest (2) spots on the receiver are predicted. This is clearer when an image from the thermal imaging camera is compared to the thermal contours in Figure 9 and Figure 10.

Table 3: Experiment 2 data.

Thermocouple	1	2	3	4	5
Experimental (shadow)	318.5	318.0	313.0	315.6	384.0
Experimental (no-shadow)	327.9	326.0	324.8	324.9	-
Experimental difference	9.5	8.0	11.8	9.3	-
Model (shadow)	325.0	328.0	314.0	325.0	398.0
Model (no shadow)	346.0	346.0	345.0	345.0	-
Model difference	21.0	18.0	31.0	20.0	-

4 Conclusions

Validation data for simple radiative heat transfer models has been presented and compared to a finite element based thermal model, serving as a useful benchmark data for future modelling exercises. The Monte-Carlo method has been found to be particularly appropriate for third-surface shadowing, and the models also appear to be capturing the thermal shadowing of obstructing surfaces. The method by which convection is included has also been described.

Differences in magnitude between the experimental data and the model could be due to a number of parameters; the first and most sensitive culprit is the emissivity of the steel, which was kept at the default value of 0.85, even though the surfaces of the plates were coated with high-emissivity paint; other material properties and the heat transfer coefficients are also a potential source of difference, and work is in progress to take measurements for these samples.

Much of the future work will hinge on the validation and application to full scale models and the way in which convection is handled will play an important role in the success of these models. Furthermore, the radiative model needs to be modified to include various levels of reflection, and also the effects of spectrally and directional dependent surface reflectivity and emissivity.

Acknowledgement

The authors would like to thank the Defence, Science and Technology (DSTL) Laboratory for the funds which made this work possible.

References

[1] N. Lavery, S. Brown, J. Spittle, S. Rooks, L. Hayward, A. G. Smith, "Improved modelling capabilities of PHARO – a coupled CFD-Thermal solver for detailed platform IR prediction", Proc. 12th Annual Ground Target Modelling & Validation Conference, Michigan, USA, pp: 40-50, 7-9th August, 2001.
[2] N. Lavery, S. Brown, J. Spittle, S. Rooks, L. Hayward, A. G. Smith, "A Coupled CFD-Thermal Solver prediction system for detailed platform IR prediction", Proc. 11th Annual Ground Target Modelling & Validation Conference, Michigan, USA, pp: 168-176, 15-17th August, 2000.
[3] N. Lavery, S. Brown, J. Spittle, L. Hayward, S. Rooks, "Finite Element Radiative and Conductive Module for use with PHOENICS", 8th Int. PHOENICS User Conference, Luxembourg, 17-20th May, 2000.
[4] Holman, J.P., Heat Transfer, Fifth Edition, McGraw-Hill, 1981.
[5] K. Morgan, C. E. Thomas, C. Taylor, "Prediction of Turbulent Heat Transfer by the Finite Element Method," Numerical Methods in Heat Transfer, Vol. II, pp. 303-317, 1983.
[6] D. W. Pepper, J. Heinrich, "The Finite Element Method: Basic Concepts and Applications" Series in Computational and Physical Processes in Mechanical and Thermal Sciences, Hemisphere Publishing Corporation, 1992.
[7] A. Shapiro, "A Radiation-View-Factor Computer Code for Axisymettric, 2D Planar and 3D Geometry with Shadowing", Lawrence Livermore Labs, August 1983.
[8] R. Siegel, J. R. Howell, "Thermal Radiation Heat Transfer", Hemisphere Publishing Corporation, 3rd edition, 1992.